Opto-Electronic Advances

Article

March 2023, Vol. 6, No. 3

DOI: 10.29026/oea.2023.220101

Solvent-free fabrication of broadband WS_2 photodetectors on paper

Wenliang Zhang[1], Onur Çakıroğlu[1], Abdullah Al-Enizi[2], Ayman Nafady[2], Xuetao Gan[3], Xiaohua Ma[4], Sruthi Kuriakose[1], Yong Xie[1,4]* and Andres Castellanos-Gomez[1]*

Paper-based devices have attracted extensive attention due to the growing demand for disposable flexible electronics. Herein, we integrate semiconducting devices on cellulose paper substrate through a simple abrasion technique that yields high-performance photodetectors. A solvent-free WS_2 film deposited on paper favors an effective electron-hole separation and hampers recombination. The as-prepared paper-based WS_2 photodetectors exhibit a sensitive photoresponse over a wide spectral range spanning from ultraviolet (365 nm) to near-infrared (940 nm). Their responsivity value reaches up to ~270 mA W^{-1} at 35 V under a power density of 35 mW cm^{-2}. A high performance photodetector was achieved by controlling the environmental exposure as the ambient oxygen molecules were found to decrease the photoresponse and stability of the WS_2 photodetector. Furthermore, we have built a spectrometer using such a paper-based WS_2 device as the photodetecting component to illustrate its potential application. The present work could promote the development of cost-effective disposable photodetection devices.

Keywords: paper electronics; photodetector; van der Waals materials; solvent-free deposition; tungsten disulfide

Zhang WL, Çakıroğlu O, Al-Enizi A, Nafady A, Gan XT et al. Solvent-free fabrication of broadband WS_2 photodetectors on paper. *Opto-Electron Adv* **6**, 220101 (2023).

Introduction

Paper based electronics have gained popularity to meet the requirements of the next generation of smart instruments, especially disposable electronic devices[1]. Paper is commonly used in daily life, it is manufactured at very large scale and at low-cost and there are widespread policies and industrial processes for recycling it[2–4]. The price of common paper is ~0.1 € m^{-2}, far less than that of crystalline silicon wafers and plastic substrates, thus making paper an appealing candidate as an alternative and low-cost substrate for the construction of functional electronics[5]. Furthermore, unlike flexible polymer substrates such as polyimide (PI), polyethylene terephthalate (PET), and polydimethylsiloxane (PDMS)[6–9], the paper substrate is biodegradable[10,11]. The recyclable and biodegradable features of paper substrates provide a great potential to alleviate the electronic waste issue. Benefiting from these superior characteristics, various novel

[1]Materials Science Factory, Instituto de Ciencia de Materiales de Madrid (ICMM-CSIC), Madrid E-28049, Spain; [2]Department of Chemistry, College of Science, King Saud University, Riyadh 11451, Saudi Arabia; [3]Key Laboratory of Light Field Manipulation and Information Acquisition, Ministry of Industry and Information Technology, and Shaanxi Key Laboratory of Optical Information Technology, School of Physical Science and Technology, Northwestern Polytechnical University, Xi'an 710129, China; [4]School of Advanced Materials and Nanotechnology, Xidian University, Xi'an 710071, China.

*Correspondence: Y Xie, E-mail: yxie@xidian.edu.cn; A Castellanos-Gomez, E-mail: andres.castellanos@csic.es

Received: 29 May 2022; Accepted: 26 September 2022; Published online: 9 December 2022

paper-based electronic devices such as sensors[12,13], transistors[14,15], triboelectric nanogenerators (TENG)[16,17], solar cells[18,19], supercapacitors[20,21], and photodetectors, have been developed.

As one of the representative paper electronics, paper-based photodetectors are capable of converting optical pulses into electrical signals effectively, therefore could be used in many fields spanning optical communication, imaging, biological detection, and environmental monitoring[22–27]. Layered transition metal dichalcogenides (TMDCs) (e.g., WS_2 and MoS_2), hold high carrier mobility, a sizeable band gap of 1–2 eV, and strong light-matter interaction[28,29], which make these materials very prospective for optoelectronic devices[30]. The weak van der Waals (vdW) bonds among the adjacent layers allow bulk TMDCs crystals to be effectively exfoliated, enabling direct deposition of such layered crystals by direct abrasion against the substrate[5,31–36]. In addition, the high surface roughness and porous nature of cellulose fibers not only aid the adhesion of the deposited material but also provides a larger photoactive area for optoelectronic devices as compared to conventional planar substrates[37].

Standard printer paper is typically made up of interconnected cellulose fibers with diameters of 20–40 μm and lengths up to 2–5 mm[38]. This structure, very different from that of conventional micro-electronic substrates, makes it necessary to develop specialized manufacturing processes to integrate electronic materials onto paper substrates. Over the past decades, the majority of efforts to integrate vdW materials onto paper substrates have been focused on printing dispersions of liquid-phase exfoliated (LPE) nanosheets to form networks/films[39,40]. However, high-temperature thermal treatment (which can damage the paper substrates or the vdW films) is needed to evaporate the solvents used during liquid phase exfoliation[41,42]. On the other hand, the remaining residual surfactant molecules hamper the intimate contact between flakes of vdW materials, thus reducing the performance of the device.[43] In general, the responsivity of the photodetectors based on LPE nanosheets is in the order of 10–1000 μA W^{-1}, which limits their practical application[44,45]. Hence, it remains a challenge to establish an efficient deposition on paper for the mass production of thin films with high purity[31]. Our recent work has illustrated an improved all-dry abrasion method to deposit a wide variety of vdW materials on standard (untreated) office paper[46], making it possible to fabricate optoelectronic devices without the utilization of solvents.

This study aimed to integrate high-performance semiconductor photodetection devices on common paper substrate through the direct abrasion of photoactive WS_2 crystals. The WS_2 devices fabricated on paper exhibit a remarkable photoresponse behavior with responsivity values in the order of ~10 mA W^{-1} at a bias voltage of 10 V over a broad spectral range from ultraviolet (365 nm) to near-infrared (940 nm). As the applied bias voltage is increased, the responsivity is dramatically enhanced and reaches a maximum value of ~270 mA W^{-1} at a bias voltage of 35 V. Moreover, we demonstrate that the atmospheric oxygen molecules have a negative impact on the electrical conductivity and photoresponse performance of paper-based WS_2 photodetectors. In fact, the performance of the fabricated paper-supported WS_2 photodetectors is optimized when operated in vacuum and we thus propose to explore encapsulation techniques in future works. In addition, a WS_2 photodetector with the narrow channel distance is fabricated on paper using interdigitated Au electrodes, achieving a responsivity of ~200 mA W^{-1} at 5 V bias. Finally, we construct an optical spectrometer using a paper-based WS_2 device to demonstrate its potential application in sensitive photodetection components.

Experimental section

Materials sources

Common office copy paper (Winner Paper Co Ltd, 80 g m^{-2}) was used as a low-cost substrate without any pretreatment. Micronized WS_2 (tungsten disulfide) powder (0.6 micron APS) was purchased from Hagen Automation Ltd to serve as the photosensitive material. Graphite pencil (4B grade, ~80% graphite content) commercially available (Faber Castell) was utilized to deposit conductive electrodes for interfacing with readout electronics.

Device preparation

The paper-based WS_2 devices with graphite electrodes were fabricated as described in detail in Fig. 1(a). Using this all-dry abrasion method, the WS_2 film, with a thickness of ~20±5 μm[46] and a width of 2 mm, was prepared as the photosensitive channel. After drawing of the graphite electrodes, the length of the WS_2 channel could be reduced to ~250–500 μm using the assistance of a glass slide. For the paper-based WS_2 devices with interdigitated Au electrodes, the Au layer (100 nm) was thermally evaporated on top of the large-area deposited

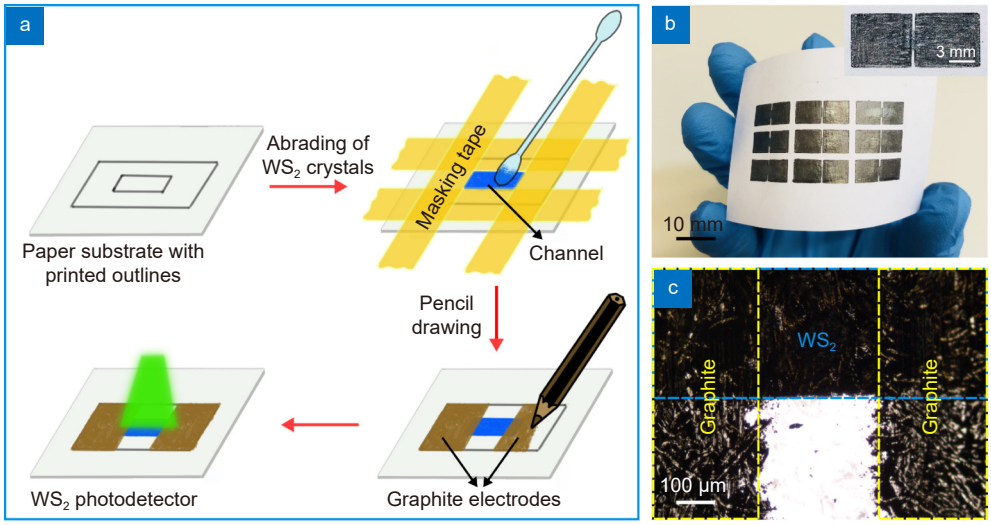

Fig. 1 | (**a**) Schematic illustration of the fabrication process of paper-based WS_2 photodetectors via abrading WS_2 crystals and penciling graphite electrodes on paper substrates. (**b**) Photograph of the 3 × 3 WS_2 photodetector array. Inset shows the magnified view of a WS_2 photodetector. (**c**) Optical micrograph of a WS_2 photodetector showing the WS_2 channel and graphite electrode regions.

WS_2 film through a patterned shadow mask (Ossila, E323) with a channel length (the space between two fingers) of 45 μm.

Photoelectric measurements

The prepared WS_2 devices were placed in a homebuilt probe station with adjustable pressure and temperature. Details about the vacuum probe station system can be found in ref.[47]. High-power fiber-coupled LEDs (Thorlabs) with different wavelengths were employed as the light source[48] to produce a light spot with a diameter of 3 mm by connecting the free-end of the multimode fiber (Thorlabs, M28L05) to a collimator. The power intensity of the output light can be regulated by a computed programmable DC power supply (Tenma 72-2710) and determined using a power meter (Thorlabs, PM100D). A Keithley-2450 source measure unit was used to measure the current vs. voltage characteristics and the temporal current response.

Results and discussion

The schematic diagram of the fabrication process of paper-based WS_2 photodetectors is shown in Fig. 1(a). The first step in device preparation is to print out the outlines of the channel and electrode on a standard copy paper with a commercial laser printer. The interior outline is then enclosed by attaching conventional masking tape to shape a rectangular mask. A continuous film is deposited onto the unmasked paper surface by simply abrading the fresh WS_2 fine crystals with a cotton swab. After the masking tape is removed, the electrode region within the exterior outline is filled by drawing with a graphite pencil of 4B grade, leaving a narrow channel for exposing the photoactive WS_2 to light illumination. Previously reported transfer length measurements showed that graphite electrodes yield low contact resistances to abraded WS_2 channels, in fact negligible in comparison to the channel resistance[46]. We address the reader to a video that shows the overall fabrication process (see Video S1 in Supplementary information). A paper-supported 3 × 3 photodetector array, as seen from the photograph in Fig. 1(b), is easily prepared through this all-dry abrasion fabrication route. This fabrication route is advantageous in avoiding the use of solvents and the high-temperature heating process. Figure 1(b) also illustrates the flexibility of paper substrates. We have recently studied similar devices to those shown in Fig. 1(b) under uniaxial tension and compression (ref.[34]) finding that the resistance of the semiconductor channel strongly depends on the applied strain: increasing with tensile strain and decreasing with compressive strain. We attribute this strain-dependent resistance to a simple phenomenon: tensile strain yields reduced overlapping area between adjacent flakes while compressive strain would increase the overlapping area. This change in flake-to-flake overlap would lead to a substantial change in the resistance of the channel. But more importantly we found that the strain-induced changes in the electrical properties of the device were reproducible and reversible, most likely due to the easy flake-to-flake sliding for van der Waals materials.

This illustrates the advantageous use of paper substrate in combination with van der Waals materials for the fabrication of flexible devices.

Figure 1(c) displays an optical micrograph of one of the prepared devices, showing the compact and continuous nature of the graphite and WS_2 films. This could be attributed to the fact that the friction force generated in the process of abrading and drawing is capable of cleaving the layered vdW crystals by breaking the weak interlayer vdW interactions, thereby forming a homogeneous coating with interconnected platelets. Interestingly, the WS_2 photoactive channel can be made as narrow as ~300 μm despite utilizing this manual "abrading/drawing" method. A recent combined scanning electron microscopy and atomic force microscopy study of abrasion-induced deposited WS_2 on polycarbonate showed that the abrasion forces experienced during the rubbing process lead to a reduction of the thickness of the WS_2 deposited flakes, from ~100–200 nm in the as-received powder to ~20–80 nm for the abraded WS_2 films[35]. We refer readers to our previous work for further characterizations on morphology and structure[46].

The photodetection performance of the paper-based WS_2 device was thoroughly investigated by measuring their electrical characteristics under dark and upon light illumination. We found that the exposure to atmospheric conditions can hamper the electrical and optoelectronic performance of the fabricated photodetectors and thus, in order to fully optimize their performance, we have studied them under high vacuum conditions. We address the reader to the Supplementary information Fig. S1 where the current is recorded during the pumping down finding a large increase of the dark current (×5) while reducing the pressure. This suggests that the ambient atmosphere may affect the electrical properties of WS_2 devices. More specifically, we found that the presence of atmospheric oxygen is the main cause of this degradation of the WS_2 performance upon air exposure (see Supplementary information Fig. S2).

To further explore the impact of ambient atmosphere on the photoresponse performance, the paper-based WS_2 device was measured under vacuum and air conditions, respectively. We subjected the WS_2 device to a periodic ON/OFF switching of light illumination at a fixed incident power density of 35 mW cm^{-2} over 100 min. As shown in Fig. 2(a) and 2(b), the current increases when the device is illuminated and then returns to the initial dark current value once the illumination is shut off. Moreover, the traces of current recorded in both vacuum and air conditions exhibit reproducible switching under 150 repeated illumination ON/OFF cycles. The significant difference is that the current trace in the vacuum condition is more stable showing only an overall smooth drift while the trace in air shows jumps. From the zoomed-in profile in Fig. 2(b), one can also observe the increment of current with lower signal-to-noise for the WS_2 device tested in vacuum as compared to that in air. These results demonstrate that the WS_2 device has better photoresponse performance in vacuum.

Response time is another essential parameter for assessing the performance of photodetection devices. The rise time at light excitation denotes the time needed for the current to climb from 10% to 90% of the photocurrent whereas the fall time in light outage represents the time taken for the current to drop from 90% to 10% of the photocurrent[49]. For the paper-based WS_2 photodetector (device A), the rise and fall time are calculated as 7.31 s and 6.58 s in vacuum, whereas in air they are 1.36 s and 1.54 s respectively.

We further determined the dependence of the photocurrent on the incident power to get a deeper insight into the photocurrent generation mechanism of the paper-based WS_2 photodetector (device A) in vacuum and air conditions. The photocurrent can be calculated by subtracting the dark current from the current under illumination condition. Fig. 2(c) plots the photocurrent of the WS_2 device as a function of time while the illumination is switched ON/OFF at increasingly high incident power intensity from 1.1 mW cm^{-2} to 35 mW cm^{-2}. Higher photocurrent is naturally obtained at higher illumination power intensities (both in air and in vacuum conditions) since higher power intensity provides a larger number of photons, enabling the formation of a larger number of electron-hole pairs[50]. Interestingly, the relationship between the photocurrent and the illumination power strongly differs when the device is measured in air and in vacuum. The relationship between the photocurrent and the incident power intensity (Fig. 2(d)) can be fitted by a power-law equation of $I_{ph} \propto P^{\alpha}$, where the exponent α specifies the photocurrent response to the incident power[51–53]. While the device tested in air show an exponent $\alpha_{Air} = 0.69$, the device in vacuum presents an exponent value of $\alpha_{Vacuum} = 0.93$. An ideal exponent of $\alpha = 1$ is expected for photoconductive photodetectors where the number of photogenerated carriers is trivially proportional to the number of incident photons. On the

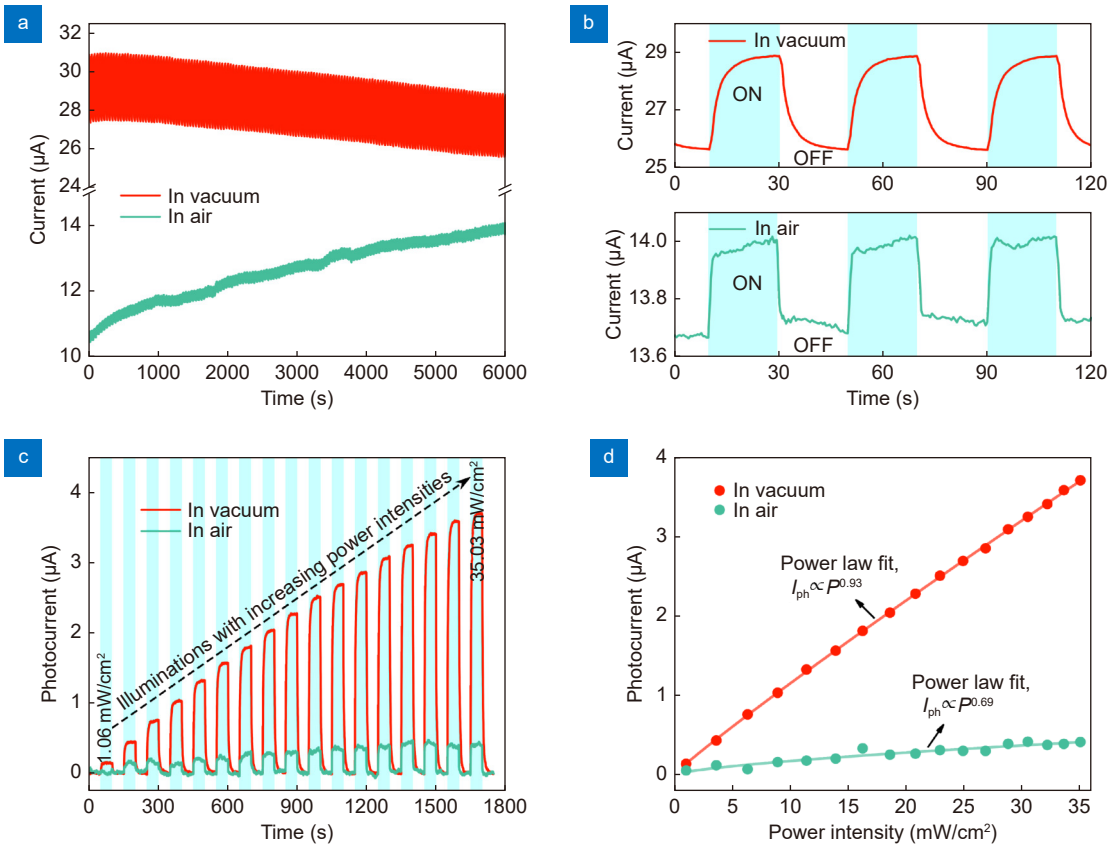

Fig. 2 | Comparison of the photoresponse performance of the paper-based WS_2 photodetector (device A) tested in air and vacuum conditions under illumination. (**a**) Current vs. time across the device under a periodic ON/OFF switching of illumination with a power intensity of 35 mW cm^{-2}. (**b**) Zoomed in on three consecutive ON/OFF cycles from (a). (**c**) Photocurrent vs. time for the WS_2 device as the illumination is switched ON/OFF with increasing incident power intensity from 1.1 mW cm^{-2} to 35 mW cm^{-2}. (**d**) Photocurrent as a function of the power intensity. Note: Measurements are carried out at a bias voltage of 10 V and with a selected wavelength of 617 nm. The channel length and width of the device A are ~300 μm and 2 mm, respectively.

other hand, the value of α less than 1 is typically observed in photodetectors, where photogating or strong carrier-dependent recombination processes play a significant role in the photocurrent generation mechanism[54]. The α_{Vacuum} value which is very close to $\alpha = 1$ points out the nearly linear dependency of the photocurrent on the incident power intensity, confirming the photoconductive nature of the all-dry deposited WS_2 photodetectors operated in vacuum.

The effect of the bias voltage on the photocurrent was further investigated by applying different bias voltages to the paper-based WS_2 photodetector (device B) for the same power-dependent measurements as mentioned above. Figure 3(a) and Fig. S3 show photocurrent vs. time at different bias voltages. The device shows a distinct power-dependent photoresponse behavior when applying the bias voltages ranging from 1 V to 35 V, which is also verified with IV curves in Fig. S4. The photocurrents as a function of incident power under various bias voltages are plotted in Fig. 3(b). The photocurrent maintains generally a near-linear relationship with the incident power even when subjected to a high voltage of 35 V. More importantly, one can observe the remarkable enhancement in photocurrent at higher voltages, which could be attributed to the increase of carrier drift velocity with stronger electrical field generated in the channel. The transit time $t_t = l^2/\mu V$, where μ is the carrier mobility, V is the bias voltage, and l is the distance between the source and drain electrodes[55]. The stronger electric field favors the separation of photoexcited electron–hole pairs and shortens the transit time, thus accelerating the charge accumulation at electrodes and increasing the photocurrent[56].

The responsivity (R) is a typical detector parameter used to compare the performance of different photodetection devices, which can be calculated as[5,57]:

$$R = \frac{I_{ph}}{P \times S_{device}}, \quad (1)$$

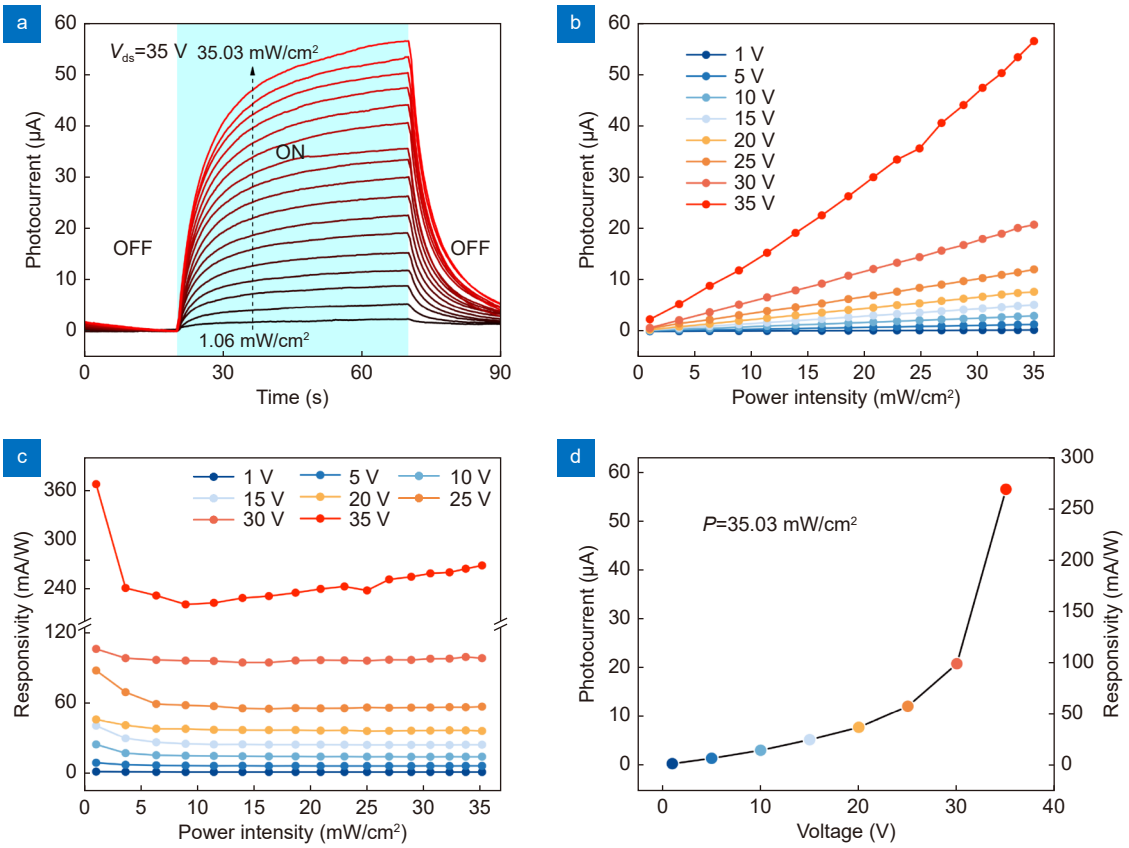

Fig. 3 | Voltage-dependent photoresponse of the paper-based WS_2 photodetector (device B) under the illumination of 617 nm. (**a**) Photocurrent as a function of time for the WS_2 photodetector while the light is switched ON/OFF under various power intensities at a fixed bias voltage of 35 V. (**b**) The measured photocurrent and (**c**) corresponding responsivity as a function of power intensity collected at various bias voltages from 1 to 35 V. (**d**) The measured photocurrent and responsivity as a function of bias voltage at a fixed power intensity of 35 mW cm^{-2}.

where I_{ph} is the generated photocurrent, P is the incident power density and S_{device} is the illuminated active channel area of the device. As plotted in Fig. 3(c), the calculated responsivity is nearly independent of the incident power (as expected as α_{Vacuum} ~1). We quantitatively compared the photocurrent and responsivity at a selected power intensity of 35 mW cm^{-2} collected at various bias voltages (Fig. 3(d)). The photocurrent (responsivity) of the paper-based WS_2 photodetector (device B) is 0.26 μA (1.2 mA W^{-1}) at 1 V and dramatically raises as the applied voltage increases, reaching a maximum of 56.5 μA (268.7 mA W^{-1}) at 35 V. On the other hand, we constructed the WS_2 device with a narrower channel length of 45 μm on paper by thermally evaporating the interdigitated Au electrodes (100 nm in thickness) and carried out identical power-dependent measurements (Fig. S5). At a bias voltage of 5 V, the WS_2 device with Au electrodes delivers a significantly enhanced responsivity of 193.9 mA W^{-1} under the same power intensity (35 mW cm^{-2}) compared with the WS_2 device with graphite electrodes (6.4 mA W^{-1}). These responsivity values measured are superior to that of other TMDCs-based photodetectors (0.018–124 mA W^{-1}) fabricated by solvent-involved approaches[37,56,58–60], and that of the WS_2 photodetectors with atomically thin layers (5×10^{-3}–12.5 mA W^{-1}) obtained through CVD[61–63], magnetron sputtering[64,65], and mechanical exfoliation methods[66]. Table 1 compares their typical device characteristics in further detail.

In order to illustrate the reproducibility of the devices fabricated by this abrasion method we measured 10 WS_2 devices with graphite electrodes at 10 V of bias voltage. The statistical results are summarized in Fig. S6. Under the illumination with a power intensity of 35 mW cm^{-2}, the photocurrent of the as-prepared WS_2 devices shows a median value of 2.6 μA and a low deviation with 50% of the devices scattering less than 1 μA. Accordingly, the responsivity of the devices presents a median of 12.7 mA W^{-1} and even reaches a maximum of ~30 mA W^{-1}. The device-to-device variation for the paper-based WS_2 photodetectors could be attributed to the percolative character of the WS_2 film since the conduction paths of charge

Table 1 | Comparison of typical device characteristics of the present WS_2 in this work and other TMDCs-based and paper-supported photodetection devices. Response time values highlighted with ^{r} or ^{f} represent the rise time and fall time values, respectively.

Material/Device	Substrate	Fabrication technique	Bias voltage (V)	Power intensity (mW cm^{-2})	Responsivity (mA W^{-1})	Response time (s)	Ref.
WS_2/Graphene	Technical paper (PEL P60)	Inkjet printing	2.5	44.1−172.6	0.61	~5	ref.[59]
Graphene(bottom)/ WS_2/Graphene(top)	Technical paper (PEL P60)	Inkjet printing	1	7	~1	–	ref.[39]
MoS_2	Paper	Rubbing process	21	7.46−111.94	0.01	~20−30	ref.[5]
ZnS-MoS_2	Paper	Hydrothermal	–	19.1	0.01785	11^r	ref.[58]
MoS_2/WSe_2	Paper	Drop cast	5	5	124	0.1^r; 0.3^f	ref.[37]
WSe_2/Ag	Photocopy paper	Rubbing process	1	0.37−0.90	0.0725	7.5	ref.[67]
WSe_2 nanodots	Filter paper	Dip coating	5	1	17.78	0.68^r; 1.01^f	ref.[56]
WSe_2/Graphite	Paper	Drop cast	1	5	6.66	0.8^r; 1.4^f	ref.[41]
ZnO/Graphene	Paper	Direct writing	–	3.9	6.27	8.76^r; 18.13^f	ref.[68]
WS_2 nanosheets	Filter membrane	Vacuum filtration	5	59.09	4.04	11.6^r; 7.9^f	ref.[60]
Multilayer WS_2	Quartz	CVD	–	–	0.092	5.3×10^{-3}	ref.[61]
WS_2	Si wafer	Drop cast	12	140	~2.5	0.03−0.07	ref.[69]
WS_2	Si wafer	Magnetron sputtering	0	15	4	1.1×10^{-6r}	ref.[65]
GOQDs-WS_2	Si wafer	Mechanical exfoliation	5	–	12.5	0.0326^r; 0.0275^f	ref.[66]
WS_2	PI	Magnetron sputtering and electron beam irradiation	10	3.9	1.66	0.48−0.86^r; 0.70−0.88^f	ref.[64]
Monolayer WS_2	PI	CVD	10	0.07	5	0.12^r	ref.[62]
WS_2	PEN	CVD	6	8.3×10^5	~5×10^{-3}	~0.08	ref.[63]
WS_2/Graphite	PET	Mechanical abrasion	2	55	24	11.8^r; 20.5^f	ref.[31]
WS_2/Graphite	Paper	All-dry abrasion	1−35	35.03	1.2 at 1 V; 6.4 at 5 V; 14.3 at 10 V; 268.7 at 35 V	7.31^r; 6.58^f	This work
WS_2/Au	Paper	All-dry abrasion	5	35.03	193.9	4.12^r; 4.14^f	This work

carriers are randomly distributed over the percolative network of interconnected WS_2 flakes.

We also studied the role of temperature in the performance of the WS_2 photodetectors. As indicated in Fig. S7, the photocurrent and responsivity both increase upon temperature increase, yielding slopes of 7.2 nA °C^{-1} and 34.3 μA W^{-1} °C^{-1}, respectively. In general, the conductivity of 2D materials is increased with higher temperature. Structural defects such as grain boundaries would also lead to large density of localized gap state. It is very likely that the mobility of WS_2 increased during heating up at high temperature[70]. Both Mott variable range hopping, and an Arrhenius-type activated transport could contribute to the conductivity of WS_2[71]. A more thorough characterization on the temperature effects of WS_2 photodetectors is beyond the scope of this paper.

The spectral responsiveness of the paper-based WS_2 photodetection device was evaluated at a fixed power intensity of 13 mW cm^{-2} using 17 high-power fiber-coupled LED sources with different wavelengths. Figure 4(a) summarizes the time-resolved photocurrent of the WS_2 photodetector (device B) in response to light stimulation with various wavelengths ranging from 365 nm (ultraviolet) to 940 nm (near-infrared). The fabricated paper-based WS_2 photodetector exhibits a broad spectral response, which could be attributed to the photon absorption capability of active WS_2 ultrathin sheets over a vast spectrum range[72]. The extracted responsivity values over different spectra ranges are shown in Fig. 4(b). The WS_2 photodetector delivers a maximum responsivity value of 14.4 mA W^{-1} at 660 nm and reduces slightly to 11.2 mA W^{-1} when the illumination wavelength exceeds 850 nm. This spectral response above 900 nm could be due to thermally activated indirect band gap absorption as multilayer WS_2 indirect gap is 1.32 eV[73]. Another plausible explanation for the broadband spectral response and the lack of strong excitonic features in the

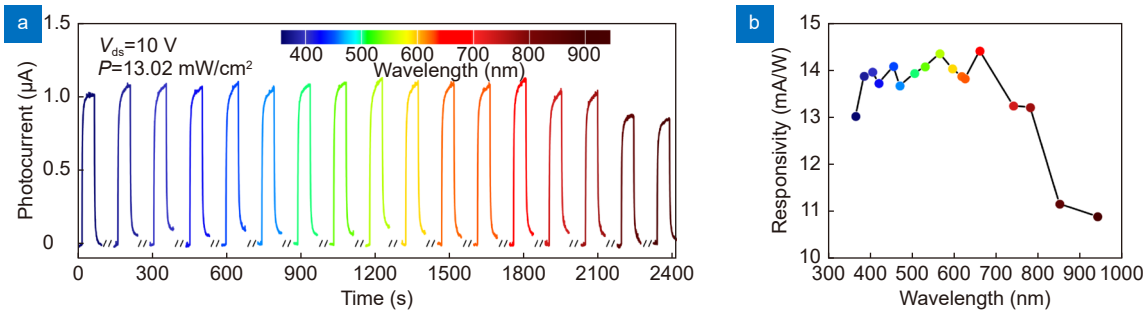

Fig. 4 | Spectral response of the paper-based WS_2 photodetector (device B). (**a**) Photocurrent vs. time when the device is subjected to cycles of ON/OFF illumination with different wavelengths. (**b**) Spectrum response of the WS_2 photodetector under various wavelengths of illumination in the range of 365 nm (ultraviolet) to 940 nm (near-infrared). Note: The device is measured at a fixed voltage of 10 V and an incident power intensity of 13 mW cm^{-2}.

photocurrent spectrum is the presence of strong bolometric effect, i.e. change in the channel resistance due to the increase of temperature induced by light absorption, in the photocurrent generation. The linear power dependence and the slower response time of the devices in vacuum further support this scenario where light would be absorbed by the graphite electrodes, even for photons with energies lower than the WS_2 bandgap, and because of the low thermal conductivity of paper substrate the WS_2 film would start to increase its temperature that would lead to a decrease of its resistance[32] and thus an increase of the current flowing through the channel.

The broad-band photodetection properties of the paper-supported WS_2 photodetector, along with the linear dependence of the photocurrent upon incident power, motivated us to explore its application in optical spectrometers. We constructed a proof-of-concept spectrometer as shown in Fig. 5(a), containing a light source, light-scattering optical element, and detection element. In this spectrometer system, a diffractive grating scatters the incoming light beam passing through a collimator into multiple wavelengths, and thereafter the light with a specific wavelength is collected with the other collimator by changing the angle of the diffractive grating. The fabricated paper-supported WS_2 device is then used to detect this selected outgoing light. Fig. 5(b) and 5(c) show the

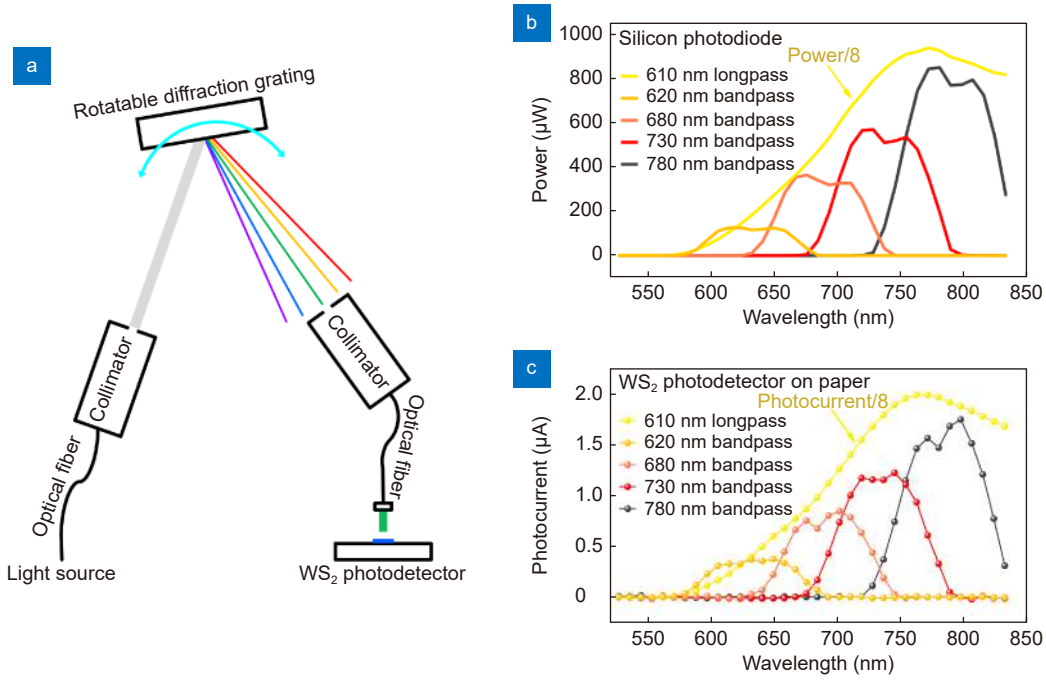

Fig. 5 | Integration of the paper-based WS_2 photodetector as detection element in an optical spectrometer. (**a**) Schematic diagram of the spectrometer system consist of a light source, a light-scattering optical element (reflective diffraction grating), and a detection element. (**b**) The measured power profiles using a commercial silicon photodiode and (**c**) photocurrent profiles using the paper-based WS_2 photodetector (device C). Note: As light source we have used a supercontinuum laser with different spectral filters.

comparison of the spectra measured using a commercial silicon photodiode (Thorlabs, PM100D) and with our paper-supported WS_2 photodetector (device C). We have used a supercontinuum laser and different spectral filters (long-pass or band-pass) to generate the test spectra to be measured with our proof-of-concept spectrometer. The remarkable agreement between the spectra measured with the commercial photodetector and our paper-supported WS_2 device suggest that our WS_2 device performs well in the quantitative detection of spectra.

Conclusions

In summary, we developed a paper-based WS_2 photodetector through a facile all-dry deposition strategy that involved the abrasion of the WS_2 photoactive channel and pencil drawing of graphite electrodes. We demonstrated that the weak van der Waals interactions between WS_2 layers allow the friction force produced during the abrasion process to cleave the layered WS_2 crystals, resulting in the formation of a uniform WS_2 film with interlinked platelets. The high purity of such an all-dry deposited WS_2 film leads to highly effective electron-hole separation and hampers the recombination. Therefore, the fabricated WS_2 photodetector shows high photoresponsivity to the incident light in a broad spectral range from ultraviolet to near-infrared. We investigated the photodetection performance of the paper-based WS_2 device in vacuum and air conditions, confirming the significant effect of oxygen molecules decreasing the photoresponse. In addition, the responsivity can be markedly improved by applying the higher biasing voltage, achieving a maximum of ~270 mA W^{-1} at a voltage of 35 V. Finally, we demonstrated the potential application of the paper-based WS_2 photodetector on spectrometers. This work paves the way for large-scale fabrication of other cost-effective electronic/optoelectronic devices.

References

1. Zhang Y, Zhang LN, Cui K, Ge SG, Cheng X et al. Flexible electronics based on micro/nanostructured paper. *Adv Mater* **30**, 1801588 (2018).
2. Xu YD, Fei QH, Page M, Zhao GG, Ling Y et al. Paper-based wearable electronics. *iScience* **24**, 102736 (2021).
3. Liu JP, Yang C, Wu HY, Lin ZY, Zhang ZX et al. Future paper based printed circuit boards for green electronics: fabrication and life cycle assessment. *Energy Environ Sci* **7**, 3674–3682 (2014).
4. Ha D, Fang ZQ, Zhitenev NB. Paper in electronic and optoelectronic devices. *Adv Electron Mater* **4**, 1700593 (2018).
5. Mazaheri A, Lee M, Van Der Zant HSJ, Frisenda R, Castellanos-Gomez A. MoS_2-on-paper optoelectronics: drawing photodetectors with van der Waals semiconductors beyond graphite. *Nanoscale* **12**, 19068–19074 (2020).
6. Yan WJ, Fuh HR, Lv YH, Chen KQ, Tsai TY et al. Giant gauge factor of Van der Waals material based strain sensors. *Nat Commun* **12**, 2018 (2021).
7. Cai WF, Wang JY, He YM, Liu S, Xiong QH et al. Strain-modulated photoelectric responses from a flexible α-In_2Se_3/3R MoS_2 heterojunction. *Nano-Micro Lett* **13**, 74 (2021).
8. Koo JH, Kim DC, Shim HJ, Kim TH, Kim DH. Flexible and stretchable smart display: materials, fabrication, device design, and system integration. *Adv Funct Mater* **28**, 1801834 (2018).
9. Miranda I, Souza A, Sousa P, Ribeiro J, Castanheira EMS et al. Properties and applications of PDMS for biomedical engineering: a review. *J Funct Biomater* **13**, 2 (2022).
10. Jung YH, Chang TH, Zhang HL, Yao CH, Zheng QF et al. High-performance green flexible electronics based on biodegradable cellulose nanofibril paper. *Nat Commun* **6**, 7170 (2015).
11. Liu HC, Jian RR, Chen HB, Tian XL, Sun CL et al. Application of biodegradable and biocompatible nanocomposites in electronics: current status and future directions. *Nanomaterials* **9**, 950 (2019).
12. Zhu PH, Kuang YD, Wei Y, Li F, Ou HJ et al. Electrostatic self-assembly enabled flexible paper-based humidity sensor with high sensitivity and superior durability. *Chem Eng J* **404**, 127105 (2021).
13. Gao L, Zhu CX, Li L, Zhang CW, Liu JH et al. All paper-based flexible and wearable piezoresistive pressure sensor. *ACS Appl Mater Interfaces* **11**, 25034–25042 (2019).
14. Jiang Z, Liu DS, Li CH, Liu HZ, Zou JH et al. Signature of *p*-type semiconductor features in paper-based back gate metal-organic framework thin-film transistors. *Appl Phys Lett* **117**, 093303 (2020).
15. Martins R, Gaspar D, Mendes MJ, Pereira L, Martins J et al. Papertronics: multigate paper transistor for multifunction applications. *Appl Mater Today* **12**, 402–414 (2018).
16. Kim I, Jeon H, Kim D, You J, Kim D. All-in-one cellulose based triboelectric nanogenerator for electronic paper using simple filtration process. *Nano Energy* **53**, 975–981 (2018).
17. Mao YC, Zhang N, Tang YJ, Wang M, Chao MJ et al. A paper triboelectric nanogenerator for self-powered electronic systems. *Nanoscale* **9**, 14499–14505 (2017).
18. Brunetti F, Operamolla A, Castro-Hermosa S, Lucarelli G, Manca V et al. Printed solar cells and energy storage devices on paper substrates. *Adv Funct Mater* **29**, 1806798 (2019).
19. Barr MC, Rowehl JA, Lunt RR, Xu JJ, Wang AN et al. Direct monolithic integration of organic photovoltaic circuits on unmodified paper. *Adv Mater* **23**, 3500–3505 (2011).
20. Zhang YZ, Wang Y, Cheng T, Lai WY, Pang H et al. Flexible supercapacitors based on paper substrates: a new paradigm for low-cost energy storage. *Chem Soc Rev* **44**, 5181–5199 (2015).
21. Ko Y, Kwon M, Bae WK, Lee B, Lee SW et al. Flexible supercapacitor electrodes based on real metal-like cellulose papers. *Nat Commun* **8**, 536 (2017).
22. Pataniya PM, Sumesh CK. WS_2 nanosheet/graphene heterostructures for paper-based flexible photodetectors. *ACS Appl Nano Mater* **3**, 6935–6944 (2020).
23. Zhang Y, Xu WX, Xu XJ, Yang W, Li SY et al. Low-cost writing method for self-powered paper-based UV photodetectors utilizing Te/TiO_2 and Te/ZnO heterojunctions. *Nanoscale Horiz* **4**,

452–456 (2019).
24. Fang HJ, Li JW, Ding J, Sun Y, Li Q et al. An origami perovskite photodetector with spatial recognition ability. *ACS Appl Mater Interfaces* **9**, 10921–10928 (2017).
25. Cai S, Zuo CL, Zhang JY, Liu H, Fang XS. A paper-based wearable photodetector for simultaneous UV intensity and dosage measurement. *Adv Funct Mater* **31**, 2100026 (2021).
26. Kannichankandy D, Pataniya PM, Zankat CK, Tannarana M, Pathak VM et al. Paper based organic–inorganic hybrid photodetector for visible light detection. *Appl Surf Sci* **524**, 146589 (2020).
27. Xie C, Yan F. Flexible photodetectors based on novel functional materials. *Small* **13**, 1701822 (2017).
28. Jiang X, Chen F, Zhao SC, Su WT. Recent progress in the CVD growth of 2D vertical heterostructures based on transition-metal dichalcogenides. *CrystEngComm* **23**, 8239–8254 (2021).
29. Nan HY, Zhou RW, Gu XF, Xiao SQ, Ostrikov K. Recent advances in plasma modification of 2D transition metal dichalcogenides. *Nanoscale* **11**, 19202–19213 (2019).
30. Huo NJ, Yang SX, Wei ZM, Li SS, Xia JB et al. Photoresponsive and gas sensing field-effect transistors based on multilayer WS_2 nanoflakes. *Sci Rep* **4**, 5209 (2014).
31. Nutting D, Felix JF, Tillotson E, Shin DW, De Sanctis A et al. Heterostructures formed through abraded van der Waals materials. *Nat Commun* **11**, 3047 (2020).
32. Lee M, Mazaheri A, Van Der Zant HSJ, Frisenda R, Castellanos-Gomez A. Drawing WS_2 thermal sensors on paper substrates. *Nanoscale* **12**, 22091–22096 (2020).
33. Matatagui D, Cruz C, Carrascoso F, Al-Enizi AM, Nafady A et al. Eco-friendly disposable WS_2 paper sensor for sub-ppm NO_2 detection at room temperature. *Nanomaterials* **12**, 1213 (2022).
34. Zhang WL, Frisenda R, Zhao QH, Carrascoso F, Al-Enizi AM et al. Paper-supported WS_2 strain gauges. *Sens Actuators A Phys* **332**, 113204 (2021).
35. Quereda J, Kuriakose S, Munuera C, Mompean FJ, Al-Enizi AM et al. Scalable and low-cost fabrication of flexible WS_2 photodetectors on polycarbonate. *npj Flexible Electron* **6**, 23 (2022).
36. Azpeitia J, Frisenda R, Lee M, Bouwmeester D, Zhang WL et al. Integrating superconducting van der Waals materials on paper substrates. *Mater Adv* **2**, 3274–3281 (2021).
37. Pataniya PM, Patel V, Sumesh CK. MoS_2/WSe_2 nanohybrids for flexible paper-based photodetectors. *Nanotechnology* **32**, 315709 (2021).
38. Tobjörk D, Österbacka R. Paper electronics. *Adv Mater* **23**, 1935–1961 (2011).
39. McManus D, Vranic S, Withers F, Sanchez-Romaguera V, Macucci M et al. Water-based and biocompatible 2D crystal inks for all-inkjet-printed heterostructures. *Nat Nanotechnol* **12**, 343–350 (2017).
40. Casiraghi C, Macucci M, Parvez K, Worsley R, Shin Y et al. Inkjet printed 2D-crystal based strain gauges on paper. *Carbon* **129**, 462–467 (2018).
41. Pataniya PM, Sumesh CK. Low cost and flexible photodetector based on WSe_2 Nanosheets/Graphite heterostructure. *Synth Met* **265**, 116400 (2020).
42. Torrisi F, Carey T. Graphene, related two-dimensional crystals and hybrid systems for printed and wearable electronics. *Nano Today* **23**, 73–96 (2018).
43. Ricardo KB, Sendecki A, Liu HT. Surfactant-free exfoliation of graphite in aqueous solutions. *Chem Commun* **50**, 2751–2754 (2014).
44. Alzakia FI, Jonhson W, Ding J, Tan SC. Ultrafast exfoliation of 2D materials by solvent activation and one-step fabrication of all-2D-material photodetectors by electrohydrodynamic printing. *ACS Appl Mater Interfaces* **12**, 28840–28851 (2020).
45. McManus D, Santo AD, Selvasundaram PB, Krupke R, LiBassi A et al. Photocurrent study of all-printed photodetectors on paper made of different transition metal dichalcogenide nanosheets. *Flex Print Electron* **3**, 034005 (2018).
46. Zhang WL, Zhao QH, Munuera C, Lee M, Flores E et al. Integrating van der Waals materials on paper substrates for electrical and optical applications. *Appl Mater Today* **23**, 101012 (2021).
47. Zhao QH, Carrascoso F, Gant P, Wang T, Frisenda R et al. A system to test 2D optoelectronic devices in high vacuum. *J Phys Mater* **3**, 036001 (2020).
48. Quereda J, Zhao QH, Diez E, Frisenda R, Castellanos-Gomez A. Fiber-coupled light-emitting diodes (LEDs) as safe and convenient light sources for the characterization of optoelectronic devices [version 1; peer review: 1 approved, 1 approved with reservations]. *Open Res Europe* **1**, 98 (2021).
49. An JN, Le TSD, Lim CHJ, Tran VT, Zhan ZY et al. Single-step selective laser writing of flexible photodetectors for wearable optoelectronics. *Adv Sci* **5**, 1800496 (2018).
50. Yang W, Hu K, Teng F, Weng JH, Zhang Y et al. High-performance silicon-compatible large-area UV-to-visible broadband photodetector based on integrated lattice-matched type II Se/n-Si heterojunctions. *Nano Lett* **18**, 4697–4703 (2018).
51. Li SY, Zhang Y, Yang W, Liu H, Fang XS. 2D perovskite $Sr_2Nb_3O_{10}$ for high-performance UV photodetectors. *Adv Mater* **32**, 1905443 (2020).
52. Wang FK, Gao T, Zhang Q, Hu ZY, Jin B et al. Liquid-alloy-assisted growth of 2D ternary $Ga_2In_4S_9$ toward high-performance UV photodetection. *Adv Mater* **31**, 1806306 (2019).
53. Huang WJ, Gan L, Yang HT, Zhou N, Wang RY et al. Controlled synthesis of ultrathin 2D β-In_2S_3 with broadband photoresponse by chemical vapor deposition. *Adv Funct Mater* **27**, 1702448 (2017).
54. Island JO, Blanter SI, Buscema M, Van Der Zant HSJ, Castellanos-Gomez A. Gate controlled photocurrent generation mechanisms in high-gain In_2Se_3 phototransistors. *Nano Lett* **15**, 7853–7858 (2015).
55. Soci C, Zhang A, Xiang B, Dayeh SA, Aplin DPR et al. ZnO nanowire UV photodetectors with high internal gain. *Nano Lett* **7**, 1003–1009 (2007).
56. Pataniya P, Zankat CK, Tannarana M, Sumesh CK, Narayan S et al. Paper-based flexible photodetector functionalized by WSe_2 nanodots. *ACS Appl Nano Mater* **2**, 2758–2766 (2019).
57. Ouyang WX, Teng F, Fang XS. High performance BiOCl nanosheets/TiO_2 nanotube arrays heterojunction UV photodetector: the influences of self-induced inner electric fields in the BiOCl nanosheets. *Adv Funct Mater* **28**, 1707178 (2018).
58. Gomathi PT, Sahatiya P, Badhulika S. Large-area, flexible broadband photodetector based on ZnS–MoS_2 hybrid on paper substrate. *Adv Funct Mater* **27**, 1701611 (2017).
59. Leng T, Parvez K, Pan KW, Ali J, McManus D et al. Printed graphene/WS_2 battery-free wireless photosensor on papers. *2D Mater* **7**, 024004 (2020).
60. Li JY, Han JF, Li HX, Fan XY, Huang K. Large-area, flexible broadband photodetector based on WS_2 nanosheets films.

Mater Sci Semicond Process **107**, 104804 (2020).
61. Perea-Lõpez N, Elías AL, Berkdemir A, Castro-Beltran A, Gutiérrez HR et al. Photosensor device based on few-layered WS_2 films. *Adv Funct Mater* **23**, 5511–5517 (2013).
62. Lan CY, Zhou ZY, Zhou ZF, Li C, Shu L et al. Wafer-scale synthesis of monolayer WS_2 for high-performance flexible photodetectors by enhanced chemical vapor deposition. *Nano Res* **11**, 3371–3384 (2018).
63. Tweedie MEP, Lau CS, Hou L, Wang X, Sheng Y et al. Transparent ultrathin all-two-dimensional lateral Gr: WS_2: Gr photodetector arrays on flexible substrates and their strain induced failure mechanisms. *Mater Today Adv* **6**, 100067 (2020).
64. Kim BH, Yoon H, Kwon SH, Kim DW, Yoon YJ. Direct WS_2 photodetector fabrication on a flexible substrate. *Vacuum* **184**, 109950 (2021).
65. Kim HS, Patel M, Kim J, Jeong MS. Growth of wafer-scale standing layers of WS_2 for self-biased high-speed UV-visible-NIR optoelectronic devices. *ACS Appl Mater Interfaces* **10**, 3964–3974 (2018).
66. Li HJW, Huang K, Zhang YZ. Enhanced photoresponsivity of the GOQDs decorated WS_2 photodetector. *Mater Res Express* **6**, 045902 (2019).
67. Patel RP, Pataniya PM, Patel M, Sumesh CK. WSe_2 crystals on paper: flexible, large area and broadband photodetectors. *Nanotechnology* **32**, 505202 (2021).
68. Veerla RS, Sahatiya P, Badhulika S. Fabrication of a flexible UV photodetector and disposable photoresponsive uric acid sensor by direct writing of ZnO pencil on paper. *J Mater Chem C* **5**, 10231–10240 (2017).
69. Abid, Sehrawat P, Islam SS. Broadband photodetection in wide temperature range: layer-by-layer exfoliation monitoring of WS_2 bulk using microscopy and spectroscopy. *J Appl Phys* **125**, 154303 (2019).
70. Cui Y, Xin R, Yu ZH, Pan YM, Ong ZY et al. High-performance monolayer WS_2 field-effect transistors on High-κ dielectrics. *Adv Mater* **27**, 5230–5234 (2015).
71. Zhu WJ, Low T, Lee YH, Wang H, Farmer DB et al. Electronic transport and device prospects of monolayer molybdenum disulphide grown by chemical vapour deposition. *Nat Commun* **5**, 3087 (2014).
72. Wu D, Guo JW, Wang CQ, Ren XY, Chen YS et al. Ultrabroadband and high-detectivity photodetector based on WS_2/Ge heterojunction through defect engineering and interface passivation. *ACS Nano* **15**, 10119–10129 (2021).
73. Gusakova J, Wang XL, Shiau LL, Krivosheeva A, Shaposhnikov V et al. Electronic properties of bulk and monolayer TMDs: theoretical study within DFT framework (GVJ-2e method). *Phys Status Solidi (A) Appl Mater Sci* **214**, 1700218 (2017).

Acknowledgements

We thank Felix Carrascoso (ICMM-CSIC) for support with the metal evaporation and Hao Li (ICMM-CSIC) for his help preparing some of the schemes for the figures. This work received funding from the European Research Council (ERC) under the European Union's Horizon 2020 research and innovation program (grant agreement n° 755655, ERC-StG 2017 project 2D-TOPSENSE), the Ministry of Science and Innovation (Spain) through the project PID2020-115566RB-I00. A. C-G. AMA-E and AN extend their sincere appreciation to the Distinguished Scientist Fellowship Program (DSFP) at King Saud University for funding of this work. Y. Xie acknowledges support from the National Natural Science Foundation of China under grant No. 61704129 and No. 62011530438, and the Key Research and Development Program of Shaanxi (Program No. 2021KW-02) and Fundamental Research Funds for the Central Universities (JB211409). W. L. Zhang acknowledges the grant from China Scholarship Council (CSC) under No. 201908610178. Onur Çakıroğlu acknowledges the support from European Union's Horizon 2020 research and innovation program under the grant agreement 956813 (2Exciting).

Author contributions

W. L. Zhang fabricated the samples, performed the measurements and wrote the original manuscript. O. Çakıroğlu scripted the program for the photodetection measurement. S. Kuriakose, AMA-E and AN revised the manuscript. Y. Xie revised the manuscript and supervised the work. A. Castellanos-Gomez proposed the original idea, designed the experiments and supervised the work.

Competing interests

The authors declare no competing financial interests.

Supplementary information

Supplementary information for this paper is available at
https://doi.org/10.29026/oea.2023.220101